# High-Resolution Transmission Electron Microscopy Using Negative Spherical Aberration

Chun-Lin Jia, Markus Lentzen,* and Knut Urban

*Institut für Festkörperforschung, Forschungszentrum Jülich GmbH, 52425 Jülich, Germany*

**Abstract:** A novel imaging mode for high-resolution transmission electron microscopy is described. It is based on the adjustment of a negative value of the spherical aberration $C_S$ of the objective lens of a transmission electron microscope equipped with a multipole aberration corrector system. Negative spherical aberration applied together with an overfocus yields high-resolution images with *bright-atom* contrast. Compared to all kinds of images taken in conventional transmission electron microscopes, where the then unavoidable positive spherical aberration is combined with an underfocus, the contrast is dramatically increased. This effect can only be understood on the basis of a full nonlinear imaging theory. Calculations show that the nonlinear contrast contributions diminish the image contrast relative to the linear image for a positive-$C_S$ setting whereas they reinforce the image contrast relative to the linear image for a negative-$C_S$ setting. The application of the new mode to the imaging of oxygen in $SrTiO_3$ and $YBa_2Cu_3O_7$ demonstrates the benefit to materials science investigations. It allows us to image directly, without further image processing, strongly scattering heavy-atom columns together with weakly scattering light-atom columns.

**Key words:** aberration correction, spherical aberration, atomic resolution imaging, contrast theory, oxygen imaging, defects in electroceramics

## INTRODUCTION

In electron microscopy the traditional modes of high-resolution imaging are mainly controlled by the objective lens defocus. There are three important and generally used defocus settings: (1) Scherzer's defocus maximizing the phase-contrast of a weak-phase object (Scherzer, 1949), Lichte's defocus of least confusion (Lichte, 1991) minimizing contrast delocalization (Lichte, 1991; Coene & Jansen, 1992), and the minimum phase-contrast defocus (Heinemann, 1971). All these defocus settings are located at underfocus. This means that the appertaining image planes (for paraxial rays) are located between the objective lens and the Gaussian image plane. The reason for this is the *positive* spherical aberration of the objective lens, which has to be counterbalanced in all three cases in a certain way by a *negative* defocus aberration related to underfocus.

The defocus values are directly linked to the value of the fixed spherical aberration, and hence they are fixed, too. This has a number of drawbacks for the three imaging modes, particularly for electron microscopes equipped with a field-emission gun. The point resolution obtained at Scherzer's defocus is lower than the information limit of the instrument. At Lichte's defocus of least confusion, contrast

reversals occur introducing strong imaging artifacts, and at the minimum phase-contrast defocus, the contrast is reduced only up to a certain resolution, lower than that corresponding to the information limit.

In recent years it has been demonstrated that it is possible to compensate the spherical aberration of a transmission electron microscope by means of a corrector system consisting of two magnetic hexapole lenses and two transfer-lens doublets (Haider et al., 1998*b*). Such a system was implemented in the Jülich Philips CM 200 FEG ST equipped with a field-emission gun. Results on the optical alignment and the performance of this instrument were reported (Haider et al., 1998*a*, 1998*b*; Urban et al., 1999). By variation of the excitation of the hexapole system, the spherical aberration of the objective-lens/corrector assembly can not only be compensated to zero, it can be varied within wide limits. Operating the instrument as a variable spherical-aberration transmission electron microscope (VSATEM) the value of the spherical aberration, $C_S$, can be used as an additional parameter for optimization of high-resolution image quality and contrast. By proper tuning of $C_S$, the drawbacks of the three imaging modes mentioned above can be eliminated (Lentzen et al., 2002). The point resolution at Scherzer's defocus can be extended to the information limit; for small values of the spherical aberration, Lichte's defocus is free of contrast reversals; and for small values of the spherical aberration, minimum phase-contrast can be obtained up to the information limit. By choosing

zero spherical aberration and zero defocus, the contrast delocalization is eliminated, and a perfect minimum phase-contrast image is obtained.

Recently it was discovered that operating the VSATEM in the overcompensated mode adjusting a *negative* value of the spherical aberration and combining this with an over-focus brings about a novel high-resolution imaging mode in which the contrast of weakly scattering light atoms in the vicinity of strongly scattering heavy atoms is dramatically enhanced (Jia et al., 2003). Applying this imaging mode to the dielectric $SrTiO_3$ and the high-temperature super-conductor $YBa_2Cu_3O_7$ not only allowed us to image the oxygen-atom columns in these materials but also to quantify the local oxygen-column occupancy in unprocessed single images.

In this article we shall investigate this negative spherical aberration imaging mode in greater detail and give some more examples of its application.

## New Aspects to Imaging Theory

The imperfections of the imaging system of a microscope are characterized in the wave-optical formalism by the aberration function $\chi(g)$, which is defined by the phase deviation $2\pi\chi(g)$ of a given wavefront from an ideal wavefront, with $g$ the diffraction vector in reciprocal space. The imperfections can be equivalently characterized in the geometrical-optics formalism by the displacement of rays, $R(g)$, in the imaging plane. The aberration function and the displacement are linked by the relation $R(g) = \nabla\chi(g)$.

With the defocus aberration $Z$ and the electron wavelength $\lambda$, the aberration function and the displacement read

$$\chi(g) = \tfrac{1}{2}Z\lambda g^2 + \tfrac{1}{4}C_S\lambda^3 g^4 \tag{1}$$

and

$$R(g) = Z\lambda g + C_S\lambda^3 g^2 g. \tag{2}$$

Choosing $Z = 0$ and $C_S = 0$, the aberration function and the ray displacement are zero, and the electron wave passes the imaging system unaltered. The contrast delocalization (Lichte, 1991; Coene & Jansen, 1992)

$$R = \max|R(g)|, \quad g \le g_{max} \tag{3}$$

belonging to the information limit, characterized by the spatial frequency $g_{max}$, becomes zero, and the image intensity is equal to the intensity of the wave function $\psi(r)$ convolved with the point-spread function $p(r)$ owing to the partially coherent illumination ($r$ a vector in the image plane):

$$I(r) = |\psi(r) \otimes p(r)|^2. \tag{4}$$

In the framework of linear imaging theory, where only linear interference terms between the transmitted beam and the diffracted beams are considered whereas the interference terms between diffracted beams are neglected, the image intensity represents the amplitude modulation of the wave function owing to a weak object; the phase modulation introduced by the weak-phase object is lost.

Choosing in the VSATEM an underfocus

$$Z = -\tfrac{16}{9}(\lambda g_{max}^2)^{-1} \tag{5}$$

and a *positive* spherical aberration of

$$C_S = \tfrac{64}{27}(\lambda^3 g_{max}^4)^{-1}, \tag{6}$$

the aberration function is negative up to the information limit (Lentzen et al., 2002), yielding a broad Scherzer pass-band with a phase deviation close to $-\pi/2$. In the framework of the linear imaging theory, a weak-phase object is then imaged with *dark-atom contrast*. The delocalization takes a value of

$$R = \tfrac{16}{27}g_{max}^{-1}. \tag{7}$$

For our 200-kV Philips CM200 FEG ST, the respective values are: $Z = -11$ nm, $C_S = 37$ $\mu$m, and $R = 0.074$ nm, for an electron wavelength of 2.5 pm and an information limit of 8 nm$^{-1}$.

Choosing an overfocus

$$Z = \tfrac{16}{9}(\lambda g_{max}^2)^{-1} \tag{8}$$

and a *negative* spherical aberration

$$C_S = -\tfrac{64}{27}(\lambda^3 g_{max}^4)^{-1}, \tag{9}$$

the aberration function is now positive up to the information limit, yielding a broad Scherzer pass-band with a phase deviation close to $\pi/2$. In the framework of linear imaging theory a weak-phase object is imaged now with *bright-atom contrast*. The delocalization takes again a value of

$$R = \tfrac{16}{27}g_{max}^{-1}. \tag{10}$$

The respective values for our 200-kV Philips instrument are: $Z = 11$ nm, $C_S = -37$ $\mu$m, and $R = 0.074$ nm.

From the standpoint of the linear imaging theory, the two settings for $Z$ and $C_S$ are symmetrical: Both extend the point resolution to the information limit; both reduce the accompanying contrast delocalization; both resolve the structure under investigation with the same resolution. Considering the full formalism of nonlinear imaging theory, which takes into account not only the linear interference
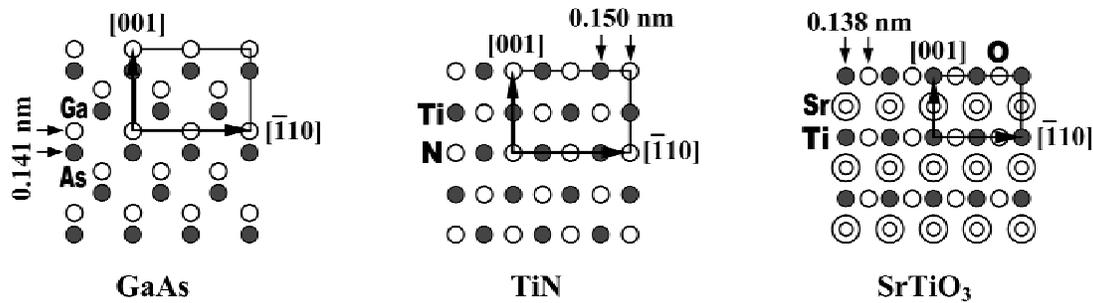
**Figure 1.** Projected structure of GaAs [110], TiN [110], and SrTiO$_3$ [110].

terms between the transmitted beam and the diffracted beams, but also the interference terms between diffracted beams, an asymmetry can be observed: Using the setting for bright-atom imaging, the resulting nonlinear modulation of the image intensity yields a higher image contrast than using the setting for dark-atom imaging.

It is quite difficult to study this nonlinear contrast phenomenon analytically, because it is based on a multibeam effect. We note that if $N$ linear interferences between the transmitted beam and the diffracted beams are considered, already $N^2$ interference terms between the diffracted beams have to be analyzed to explain the effect quantitatively. Instead a quantum-mechanical wave-optical image simulation study comprising different materials is used to throw light on the conditions for the bright-atom imaging of weakly scattering atom columns.

## SIMULATION STUDY OF THE BRIGHT-ATOM IMAGE CONTRAST

The simulation study has the objective to explore the differences between the dark-atom contrast setting, with a small positive spherical aberration and a small underfocus, and the bright-atom contrast setting, with a small negative spherical aberration and a small overfocus.

Three crystals were chosen, GaAs, TiN, and SrTiO$_3$, oriented with the electron beam parallel to [110] zone axis. The projected crystal structures are displayed in Figure 1. In these zone axes, the crystal structures have small column spacings that can be just resolved by the aberration-corrected CM200 FEG ST, which has a resolution limit of better than 0.13 nm (Lentzen et al., 2002). For each crystal structure, two defocus-thickness series of images were calculated using the Mac Tempas software package (Kilaas, 1987): one for a positive spherical aberration of 40 $\mu$m, and another for a negative spherical aberration of $-40$ $\mu$m. The maximum specimen thickness was 7.0 nm for GaAs [110], 8.0 nm for TiN [110], and 7.0 nm for SrTiO$_3$ [110]. The defocus interval ranged from 0 to $-15$ nm (underfocus) for the

positive spherical aberration, and from 0 to 15 nm (overfocus) for the negative spherical aberration. Within these defocus intervals an only moderate delocalization is introduced; larger overfoci or underfoci are not considered here, because then a higher delocalization, already in the order of intercolumn distances, would severely disturb the imaging of local column contrasts.

The defocus-thickness maps of the dark-atom contrast setting, displayed in Figures 2a, 3a, and 4a, indicate that atom columns appear dark if the specimen thickness is close to one-half of the extinction distances of the atom columns, and if an underfocus is chosen: 3.0 nm thickness and $-9.0$ nm defocus for GaAs [110], 2.0 nm thickness and $-11.0$ nm defocus for TiN [110], and 2.5 nm thickness and $-10.0$ nm defocus for SrTiO$_3$ [110]. The weakly scattering nitrogen columns of TiN and oxygen columns of SrTiO$_3$, however, are not clearly visible.

The defocus-thickness maps of the bright-atom contrast setting, displayed in Figures 2b, 3b, and 4b, indicate that atom columns appear bright if the specimen thickness is close to one-half of the extinction distances of the atom columns, and if an overfocus is chosen: 3.0 nm thickness and 10 nm defocus for GaAs [110], 4.0 nm thickness and 11.0 nm defocus for TiN [110], and 3.5 nm thickness and 11.0 nm defocus for SrTiO$_3$ [110]. The weakly scattering nitrogen columns of TiN and oxygen columns of SrTiO$_3$ are now clearly visible.

A comparison of the corresponding dark-atom and bright-atom structure images shows that the bright-atom setting generates a higher image contrast than the dark-atom setting, and the former setting is beneficial in particular to the imaging of the weakly scattering atom columns. Both settings are quite robust with respect to specimen thickness and defocus: A thickness change of a few nanometers, which is a small fraction of the extinction distances of the different atom columns, does not change contrast much, as well as a defocus change of 2 nm, which results in a phase change of the aberration function of $\pi/4$ at the information limit.

The simulation study indicates that the underlying contrast mechanism is the nonlinear imaging process. Both
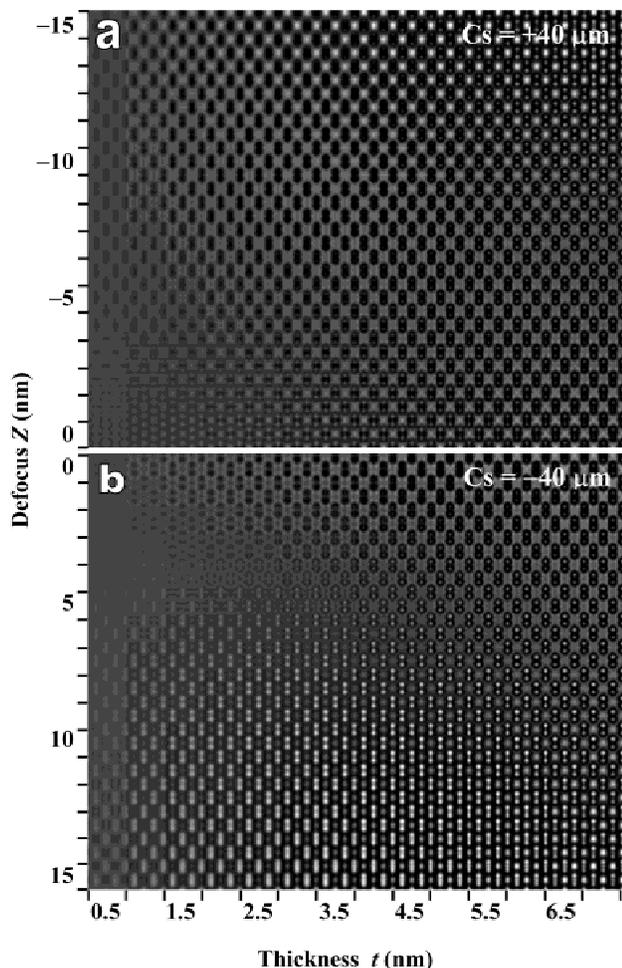
**Figure 2.** Defocus-thickness map of simulated images of GaAs [110]. **a:** Spherical aberration $C_S = 40 \ \mu$m, defocus from 0 to $-15$ nm (underfocus), thickness from 0.5 nm to 7.0 nm. **b:** Spherical aberration $C_S = -40 \ \mu$m, defocus from 0 to 15 nm (overfocus), specimen thickness from 0.5 nm to 7.0 nm.

**Figure 3.** Defocus-thickness map of simulated images of TiN [110]. **a:** Spherical aberration $C_S = 40 \ \mu$m, defocus from 0 to $-15$ nm (underfocus), thickness from 1.5 nm to 8.0 nm. **b:** Spherical aberration $C_S = -40 \ \mu$m, defocus from 0 to 15 nm (overfocus), specimen thickness from 1.5 nm to 8.0 nm.

sets of simulations, for the positive and the negative spherical aberration, were calculated for the same resolution limit, which is defined by the transfer of the linear contributions to the image intensity. Hence the influence of the linear interferences on the image contrast is the same in both cases. The linear contributions to the image intensity alone, however, would generate for the bright-atom setting merely an inverted version of the structure image taken under dark-atom imaging conditions.

The values for the spherical aberration used in this study and the defocus values for optimum dark-atom or bright-atom imaging are quite close to the values found analytically in the previous section, with deviations dependent on the material under investigation. Differences occur due to the nonlinear contributions to the image intensity, which are neglected in the analytical treatment using the linear imaging theory, and due to the deviation of a thick
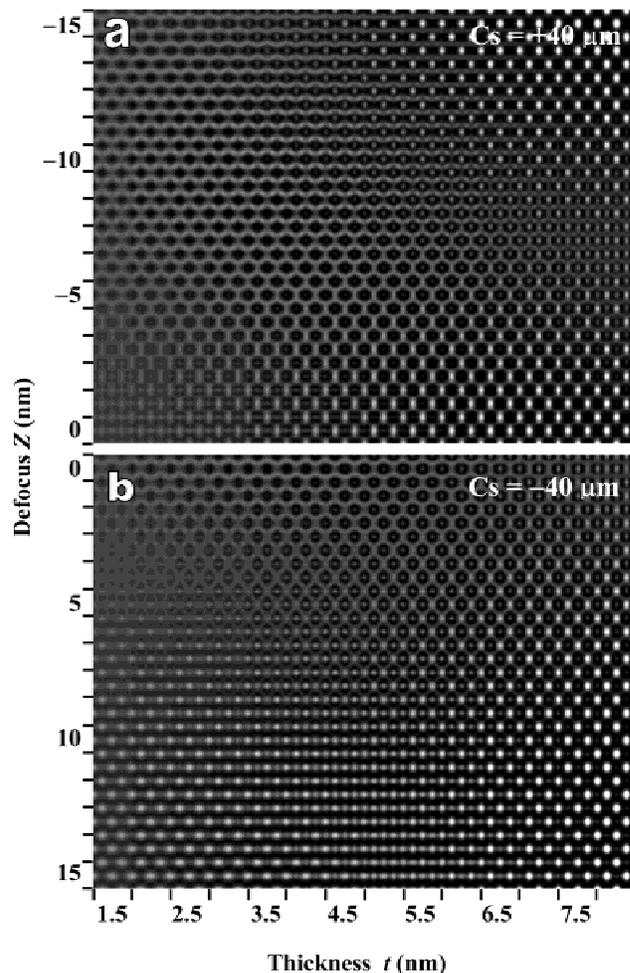
sample from the weak-phase object approximation used in the analytical treatment. The values found analytically are, however, a good guide to finding the optimum conditions for bright-atom high-resolution imaging, which can then be refined for a given material using image simulations.

Using the weak phase object approximation, a crude argument can be found for the high bright-atom contrast compared with the dark-atom contrast. The exit wave function for a thin specimen with thickness $t$,

$$\psi(\boldsymbol{r}) \approx 1 + \pi i \lambda U(\boldsymbol{r}) t, \tag{11}$$

is linear in the projected potential $U(\boldsymbol{r})$. Then wave function in the image plane is

$$\psi'(\boldsymbol{r}) \approx 1 - \pi \lambda U(\boldsymbol{r}) t, \tag{12}$$
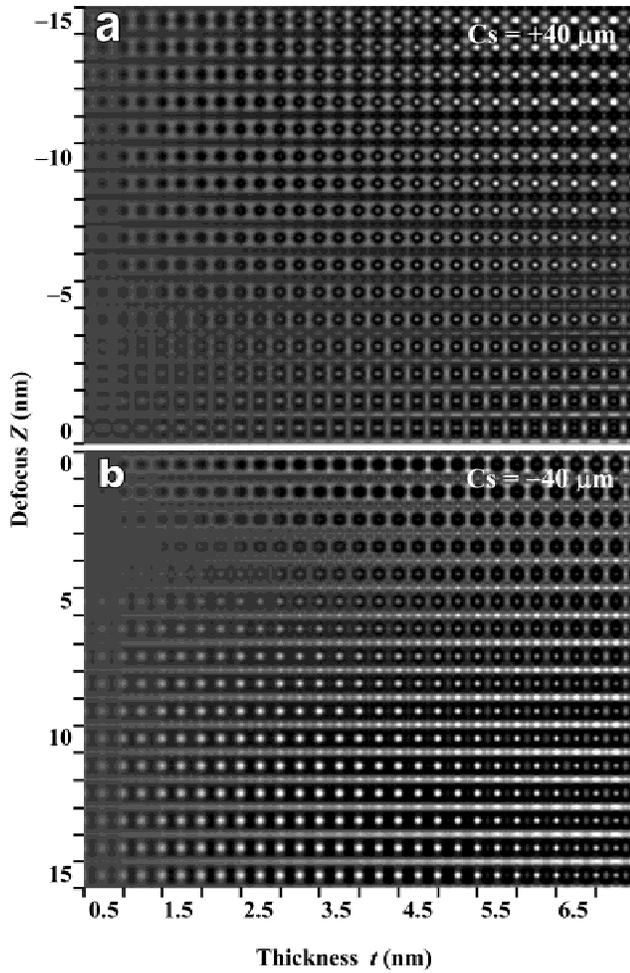
**Figure 4.** Defocus-thickness map of simulated images of SrTiO$_3$ [110]. **a:** Spherical aberration $C_S = 40$ $\mu$m, defocus from 0 to $-15$ nm (underfocus), thickness from 0.5 nm to 7.0 nm. **b:** Spherical aberration $C_S = -40$ $\mu$m, defocus from 0 to 15 nm (overfocus), specimen thickness from 0.5 nm to 7.0 nm.

if the objective lens adds a phase of $\pi/2$ to the diffracted wave, with the image intensity

$$I(\boldsymbol{r}) \approx 1 - 2\pi\lambda U(\boldsymbol{r})t + (\pi\lambda U(\boldsymbol{r})t)^2, \qquad (13)$$

which is correct to the second order in $U(\boldsymbol{r})$. If the objective lens adds a phase of $-\pi/2$ to the diffracted wave, the wave function in the image plane is

$$\psi'(\boldsymbol{r}) \approx 1 + \pi\lambda U(\boldsymbol{r})t, \qquad (14)$$

with the image intensity

$$I(\boldsymbol{r}) \approx 1 + 2\pi\lambda U(\boldsymbol{r})t + (\pi\lambda U(\boldsymbol{r})t)^2, \qquad (15)$$

again correct to the second order in $U(\boldsymbol{r})$. The contrast modulation due to the projected potential $U(\boldsymbol{r})$ in (15) is

higher than in (13), because the linear and quadratic contribution have the same sign. The additional phase of $-\pi/2$ is achieved by a positive aberration function $\chi(\boldsymbol{g})$ (see (1)), through a positive defocus $Z$ and negative spherical aberration $C_S$ (see (8) and (9)).

This treatment, however, has a number of shortcomings: expansion (11) is only valid for very thin specimens, the phase introduced by the action of defocus and spherical aberration is not constant for all scattering vectors $\boldsymbol{g}$, and the linear and nonlinear damping envelopes due to the partially coherent illumination are neglected.

The gain of contrast due to the quadratic term in (15) is, however, very small, because the linear term is assumed to be small due to the use of the weak-phase approximation. In an experiment, the sample thickness is at least a few nanometers, and the weak-phase approximation is no more valid. Then the only means to elucidate the superposition of linear and quadratic interferences is the use of an image simulation comprising a full dynamical calculation of electron scattering and the contrast transfer under partially coherent illumination.

A comparison of the linear image intensity (Fig. 5a) and the full nonlinear image intensity (Fig. 5b) for the case of SrTiO$_3$ [110] demonstrates how the linear and nonlinear interference terms reinforce the image contrast through the superposition with the same sign. The two images were calculated for a specimen thickness of 4 nm, a defocus of 8 nm, and a spherical aberration of $-40$ $\mu$m, using the linear and nonlinear imaging subroutines of the EMS simulation package (Stadelmann, 1987). Both simulations contain a full dynamical simulation of electron scattering. The linear image retains only the linear interference of the transmitted and the scattered waves, the nonlinear image both the linear and quadratic interferences.

Also, the simulation example shows that for a thick sample the quadratic interferences reinforce the linear interferences, as in the analytical treatment of the weak-phase object. An analytical treatment in closed form is, however, not possible, particularly because the damping envelopes of the quadratic interferences require a complicated investigation in reciprocal space coordinates. Despite its weakness, expansion (15) may nevertheless serve as an analogue, not more, for the complicated contrast formation for a thick sample.

## IMAGING OF WEAKLY SCATTERING ATOM COLUMNS

The above image simulation study shows that high-resolution imaging using a negative spherical aberration together with an overfocus improves the detection of weakly scattering atom columns that are close to strongly scattering atom columns, compared to traditional high-resolution electron microscopy with a positive spherical aberration or a strong
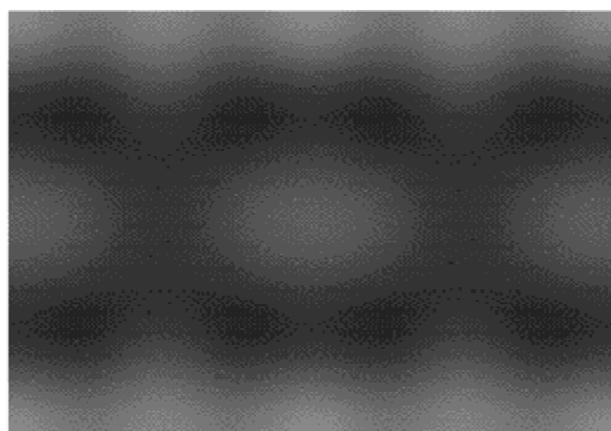
(a)
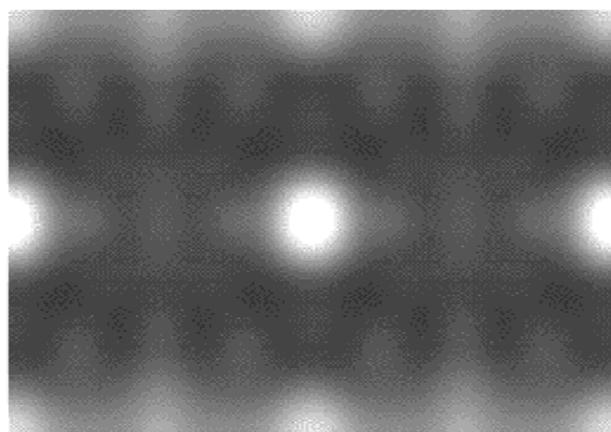


(b)

**Figure 5.** Simulated images of SrTiO$_3$ [110] for a specimen thickness of 4 nm, a spherical aberration of $-40$ $\mu$m, and a defocus of 8 nm, using (**a**) the linear image formation theory, or (**b**) the nonlinear image formation theory.

contrast delocalization or both. Both traditional microscopy and the imaging with small amounts of spherical aberration exploit the principle of favorable phase contrast, that is, the use of lens aberrations, to detect atom column structures, but the imaging mode shown in this work has two peculiarities, which are described now in more detail: (1) a low amount of aberration and hence delocalization, (2) higher contrast, if the aberration acting on the scattered wave is chosen to be positive.

Why is the detection of weakly scattering columns improved? Two contributions have to be considered closer now: the detection of object details with respect to the noise present in high-resolution images and the contrast delocalization.

Experimentally recorded images contain noise, and hence the intensity modulation owing to the local object structure can only be detected if it exceeds the noise level. Traditional high-resolution microscopy is bound to the

imaging modes linked to the strong positive spherical aberration and the appertaining underfocus settings. With these imaging modes, the nonlinear contrast contributions do not much increase the local image intensity: Strongly scattering columns still give rise to a strong modulation of the image intensity, at least via the linear contrast contributions; the contrast contributions owing to weakly scattering columns, however, may fall below the noise level and therefore cannot be detected anymore.

Using now the bright-atom imaging mode, with a negative spherical aberration and an appertaining overfocus, improves the contrast via the nonlinear contribution to the image intensity: Strongly scattering columns are imaged even stronger, the contrast contributions owing to weakly scattering columns are now increased beyond the noise level, and the weakly scattering parts of an object can be imaged successfully.

Excepting the aberration-free mode using zero defocus and zero spherical aberration, all images of an object structure are disturbed by contrast delocalization. Let us now suppose an object structure comprising two neighboring atom columns: Contrast delocalization gives rise to an intensity modulation in the vicinity of each column, and the intensity at both column locations may increase or decrease, depending on the constructive or destructive interference of the partial electron waves owing to the individual columns. The local intensity distribution is determined by the column distance and the scattering power of each column. If now one column has a much larger scattering power than the other, the mutual contributions to the local intensity distribution will affect the contrast of the weakly scattering column more strongly than the contrast of the strongly scattering column.

The effect of the contrast delocalization is, in particular, disturbing, if the column spacing is close to the information limit of the microscope. Then the columns are just resolved and any additional contrast delocalization will deteriorate the local view of the object structure. From our experimental experience with the aberration-corrected prototype, which has an information limit of better than 0.13 nm, the imaging of weakly scattering columns surrounded by strongly scattering columns is successful if the column spacings are equal to or larger than 0.14 nm.

A simulation study of the detection of the weakly scattering oxygen columns in SrTiO$_3$ illustrates the above analysis: A set of high-resolution images, displayed in Figure 6a, of strontium titanate in the [110] projection was simulated using a spherical aberration of $-40$ $\mu$m, an overfocus of 8 nm, and a specimen thickness of 4 nm. The strong contrasts belong to the Sr-O columns, the slightly weaker contrasts to the Ti columns, and the weak contrasts to the O columns. The oxygen occupancy in one of the O columns was varied from zero occupancy to full occupancy in steps of 20%. The intensity traces, displayed in Figure 6b, were extracted from the simulated images at the location of the O column along the [100] direction.
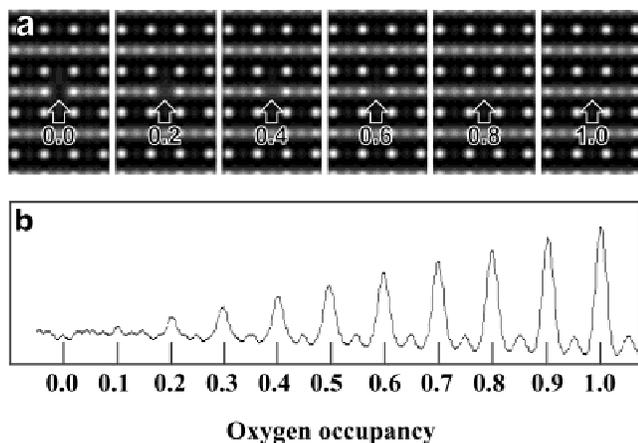
**Figure 6. a:** Series of simulated images of $SrTiO_3$ [110] with a specimen thickness of 4 nm, a spherical aberration of $-40$ $\mu$m, and a defocus of 8 nm. The oxygen occupancy of the center atom column is varied from zero (left image) to full occupancy (right image) in steps of 20%. **b:** Intensity traces across the center atom column position along [001] from zero to full oxygen occupancy in steps of 10%.

The intensity modulation at the oxygen column position grows almost linearly with the oxygen content. Compared to the small intensity variations across the projected unit cell that are related to delocalization and not to the object structure, the intensity modulation at the oxygen column position is significant for an oxygen content of 30% or larger. This is corresponding to a scattering power of the single oxygen column owing to 14 oxygen atoms distributed over a thickness of 4 nm.

## MATERIALS SCIENCE APPLICATIONS

Thin films of Ba- and Sr-based perovskites have a great potential for application as high-permittivity dielectrics in microelectronics or nonvolatile memory devices. Lattice defects and the variations of the chemical composition have an influence on the materials properties and hence also the device performance (Waser, 1997; Tagantsev et al., 2001). In particular, cation disorder and lattice strain affect the local oxygen content. The same applies to the cuprate high-temperature superconductors, which have perovskite-derived structures: The oxygen occupancy of certain lattice sites controls sensitively the charge carrier density in the superconducting planes (Jorgensen et al., 1987; Poole et al., 1995).

In the past, a number of investigations have been devoted to the determination of oxygen occupancy and oxygen ordering using medium-voltage high-resolution transmission electron microscopy. Suitable imaging condi-

tions for the detection of oxygen in $YBa_2Cu_3O$ were found using image simulation studies (Huxford et al., 1987; Ourmazd & Spence, 1987; Krekels et al., 1991; Yan & Blanchin, 1991). These imaging conditions admit the detection of the long-range superlattice ordering of oxygen vacancies, which was indeed detected experimentally (Huxford et al., 1987; Ourmazd & Spence, 1987; Yan & Blanchin, 1991; Van Tendeloo & Krekels, 2000). The special defocus conditions have, however, a large delocalization, leading to broad modulated contrast bands at the location of the copper oxide planes. The intensity modulation is controlled by copper and oxygen columns together, and hence the small contrast contribution of oxygen columns is overwhelmed by the delocalized contrast contribution of the copper columns. The oxygen occupancy therefore could not be determined locally on the scale of single atom columns.

Using high-voltage high-resolution electron microscopy Horiuchi et al. (1991) resolved in $ZrO_2$ [001] the weakly scattering oxygen sublattice together with the strongly scattering Zr sublattice. They chose Scherzer defocus imaging conditions leading to high-resolution dark-atom contrast: The combination of the instrumental parameters of the Hitachi H-1500 used in their study, a spherical aberration of 2.05 mm and a wavelength of 0.87 pm at 1000 kV, yielded a point resolution of 7.93 $nm^{-1}$, equivalent to 0.126 nm in real space. However, an investigation of oxygen columns in $YBa_2Cu_3O_7$ [010] did not yield interpretable contrast.

Using the focus-variation method, the amplitude and phase modulation of the electron wave owing to weakly and strongly scattering atom columns can be extracted from a defocus series of typically 15 to 20 images: An early application of the method by Coene et al. (1992) revealed light and heavy atoms in $YBa_2Cu_4O_8$ [100] and $Ba_2NaNb_5O_{15}$ [001], with a resolution limit of 0.14 nm and delocalization absent; a more recent one by Jia and Thust (1999) revealed the Ti and Ba-O planes, as well as single oxygen columns at a $\Sigma 3$ {111} twin boundary in $BaTiO_3$ [110], with a resolution limit of 0.15 nm and delocalization absent as well.

A problem occurs if materials consisting of both light and heavy atoms are investigated using high-resolution scanning transmission electron microscopy: Owing to the contrast mechanism of the high-angle annular dark-field technique used (Pennycook et al., 1997), only the cation sublattice consisting of strongly scattering atoms could be imaged in a recent study of $SrTiO_3$ and $LaTiO_3$ superlattices, but not the weakly scattering atoms of the oxygen sublattice (Ohtomo et al., 2002).

For our work, we used the Jülich Philips CM200 FEG ST with double-hexapole spherical-aberration corrector to investigate the oxygen occupancy and ordering in $SrTiO_3$ and $YBa_2Cu_3O_7$. The corrector was adjusted for a residual spherical aberration of $-40$ $\mu$m, which allows the recording of high-resolution bright-atom contrast images at a suitable overfocus of 8 nm with an information limit of better than 0.13 nm and a contrast delocalization of around 0.07 nm.
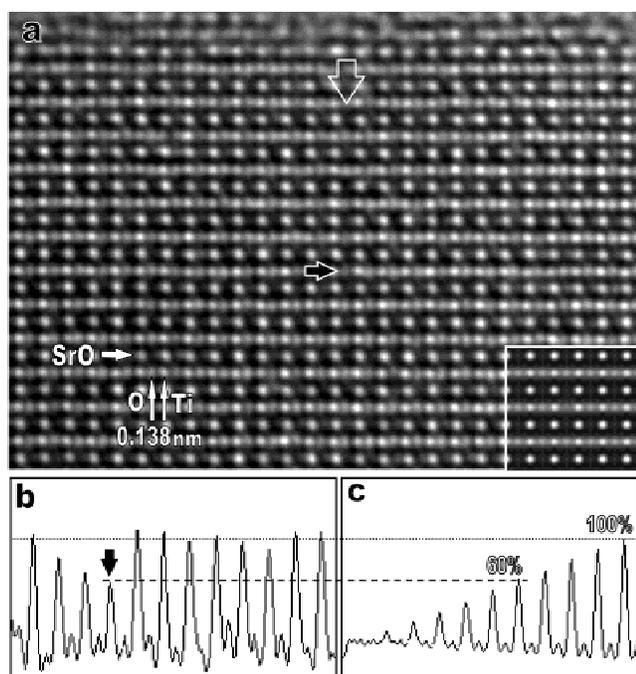
**Figure 7.  a:** Experimental image of SrTiO$_3$ [110]. The inset shows a simulated image with a specimen thickness of 4 nm, a spherical aberration of $-40$ $\mu$m, and a defocus of 8 nm. At the oxygen column marked with the black arrow, the local intensity is reduced. **b:** Intensity trace along the [001] direction indicated by the open arrow in a: The oxygen column marked with the black arrow shows a local intensity matching that of the column with an occupancy of 60% as shown in the simulated intensity trace (**c**).



**Figure 8.** Experimental images of two different edge dislocations in SrTiO$_3$ [110] with a spherical aberration of $-40$ $\mu$m and a defocus of around 8 nm.

The image displayed in Figure 7a of SrTiO$_3$, aligned with the [110] zone axis parallel to the electron beam, reveals all atom columns resolved: a strong bright contrast at the Sr-O columns, a slightly weaker bright contrast at the Ti columns, and an even weaker bright contrast at the O columns. The smallest column distance of 0.138 nm, between the Ti columns and the O columns, is clearly resolved. Because the smallest column spacing is larger than the information limit and the contrast delocalization is low, intensity modulations are related to the local atom column structure. Indeed individual oxygen columns show different local contrast, and this is a means to study the local oxygen occupancy of the columns. At the position marked with the black arrow, the oxygen-column contrast is weaker than at the surrounding oxygen columns. An intensity trace, displayed in Figure 7b, taken from the experimental image along the [001] direction, indicated by the open arrow in Figure 7a, can be compared to an intensity trace, displayed in Figure 7c, taken from simulated images. The column marked with the black arrow shows an image intensity matching that of the column with an oxygen occupancy of 60% in the calculated image.
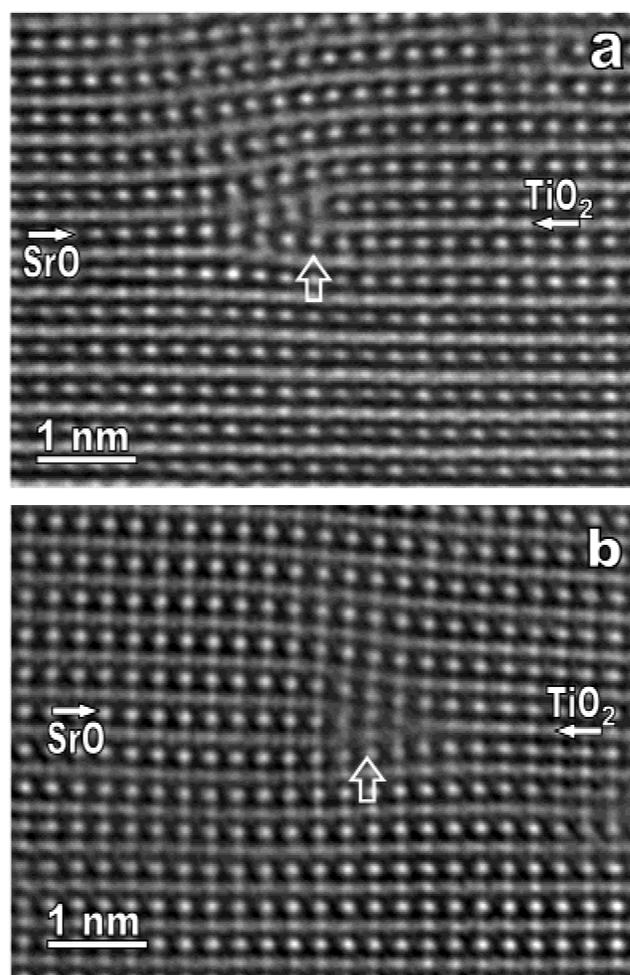
The images displayed in Figure 8a,b of SrTiO$_3$, aligned with the [110] zone axis parallel to the electron beam, reveal two different edge dislocations with a Burgers vector of the type $a$ [001]. All atom columns are resolved, and the SrO planes and the TiO$_2$ planes can be identified via the oxygen sublattice. The oxygen sublattice can be now used as a fingerprint for the two different planes to investigate the two dislocation cores. At the dislocation core, visible in the image displayed in Figure 8a, a TiO$_2$ plane and a SrO plane terminate: The TiO$_2$ plane terminates to the right-hand side of the core and the SrO plane extends into the core region by two (110) lattice spacings. The dislocation core is therefore Sr rich, which has consequences for the local oxygen content. More details, like a possible oxygen deficiency or a possible distortion of the oxygen octahedra, are not clearly visible due to the strong lattice distortions. At the dislocation core, visible in the image displayed in Figure 8b, a TiO$_2$ plane and a SrO plane terminate: The SrO plane terminates to the left-hand side of the core, and the TiO$_2$ plane extends
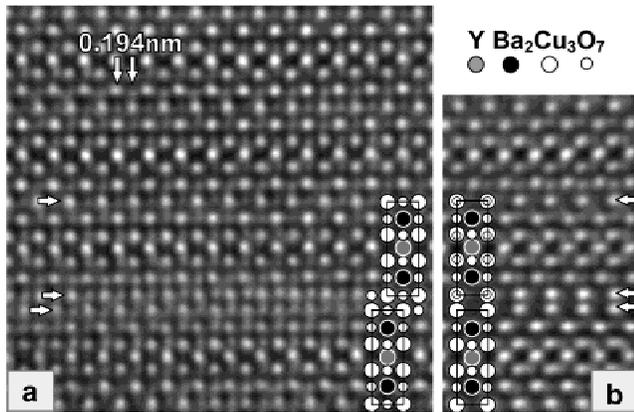
**Figure 9. a:** Experimental image of a stacking fault in $YBa_2Cu_3O_7$ [100] with a spherical aberration of $-40$ $\mu m$ and a defocus of around 12 nm. **b:** Experimental image of a stacking fault in $YBa_2Cu_3O_7$ [010] with spherical aberration of $-40$ $\mu m$, and a defocus of 12 nm.

into the core region. The dislocation core is therefore Ti rich, which again has consequences for the local oxygen content. More details are again not clearly visible due to the strong lattice distortions.

The two images displayed in Figure 9a,b of $YBa_2Cu_3O_7$ were taken with the [100] zone axis and with the [010] zone axis parallel to the electron beam. All atom columns are resolved, with strong bright contrasts at the projected cation positions and weak contrasts at the oxygen column positions. Both images reveal a stacking fault consisting of a double copper-oxide layer, marked with double arrows. The two images, taken at different specimen locations, show the structure at two different orientations, tilted by 90° with respect to the vertical axis. The image displayed in Figure 9a reveals in the [100] zone axis orientation single copper and oxygen columns in the copper-oxide-chain plane, denoted with a single arrow, and between the double copper-oxide-chain planes of the stacking fault, denoted with double arrows, a shift by one-half of the (010) lattice parameter. The image displayed in Figure 9b reveals in the [010] zone axis orientation single copper-oxygen columns in the copper-oxide-chain planes, and in this projection no shift between the two copper-oxide planes can be seen: The two crystals are translated purely along the [010] direction. This occurrence of a copper-oxide double-layer is called a "124" fault, because periodic arrangements of such faults form the structure of $YBa_2Cu_4O_8$ (Zandbergen et al., 1988; Coene et al., 1992). A close look at the intensity related to the oxygen column positions in the two structure projections reveals a strong oxygen ordering in the copper-oxide double plane: Copper-oxide chains are formed along the [010] direction, which can be explained by particularly strong copper-oxygen bonds along that direction (Morris et al., 1989).

## DISCUSSION

The above sections have thrown light on the contrast mechanism of the bright-atom imaging mode using a small negative spherical aberration and a small overfocus. This mode turned out to be beneficial for the imaging of weakly scattering atom columns through exploiting the nonlinear image formation in the transmission electron microscope. Still, a few questions remain, which are discussed now.

How general can the new bright-atom imaging mode be used? Considering the underlying nonlinear contrast mechanism, a number of limitations can be deduced: (1) The nonlinear interferences between diffracted beams are expected to be strong if the single beams already have a high amplitude. The detection of weakly scattering atom columns is therefore pronounced if the specimen thickness is approaching an odd multiple of the important extinction distances. (2) At specimen thicknesses close to an even multiple of the extinction distances, the detection may fail due to the noise contributing to the image contrast. (3) At a specimen location of interest, let us say at a dislocation core, the specimen thickness may not be favorable. These limitations are, however, not serious: The majority of quantitative high-resolution investigations fully exploiting the information limit of an instrument are carried out in thin specimen areas below the first extinction distance.

Another limitation arises from the optical principle used to create the increased contrast, namely the introduction of a positive aberration through the use of a negative spherical aberration and an overfocus: Introducing an aberration is linked to introducing a delocalization, which spreads contrast contributions in the image plane. Atom columns that should be resolved considering the information limit of the instrument alone may not appear well separated in the image due to the additional delocalization. Hence, the useful range of column distances is limited by the information limit plus a fraction of the delocalization: The increased bright-atom image contrast is gained at the cost of not fully exploiting the information limit of the microscope. Using the focus-variation method, the useful range of column distances is larger, because the delocalization is removed at the cost of taking a series of images instead of a single image.

A third limitation can be given already by the object structure under investigation, when the relative scattering power of adjacent columns differs strongly: Even if the column distances are well resolved, delocalized contrast contributions of a strongly scattering column may still overwhelm the local contrast at a weakly scattering column position.

How precise is the method of using the bright-atom contrast setting? Experimental conditions, like the relation of the local intensity modulation, owing to the scattering power of an atom column, to the noise present in images have been discussed already in the above sections, as well

as thickness and defocus variations. The alignment of the microscope has to be as precise as in any other traditional high-resolution work: Deviations from the beneficial bright-atom contrast setting can be measured, for example, by the $\pi/4$ criterion, which demands the phase change due to a single aberration to be less than $\pi/4$ at the information limit. Limits to the defocus, $\delta Z$, and the spherical aberration, $\delta C_S$, are then

$$\delta Z = \tfrac{1}{4}(\lambda g_{\max}^2)^{-1} \tag{16}$$

and

$$\delta C_S = \tfrac{1}{2}(\lambda^3 g_{\max}^4)^{-1}. \tag{17}$$

The respective values for our corrected instrument are: $\delta Z = 1.6$ nm and $\delta C_S = 7.8$ $\mu$m.

## Conclusion

In his article from 1949, "The Theoretical Resolution Limit of the Electron Microscope," O. Scherzer investigated the conditions under which single atoms should be directly visible in the electron microscope. He took into account not only the resolution limit but also the contrast in the image, and he concluded that the imaging of weakly scattering atoms, such as carbon, using an *optimal focus*, which we call nowadays Scherzer's defocus, should be possible with a resolution limit of 0.2 nm.

The instrumental development in transmission electron microscopy has already achieved resolution limits much better than this (Kisielowski et al., 2001; O'Keefe et al., 2001). Yet the high spherical aberration prevented the use of appropriate imaging conditions, excepting those possible in high-voltage microscopy, to generate a local contrast high enough to image light atoms in the vicinity of heavy atoms directly.

With the aberration-corrected transmission electron microscope (Rose, 1990; Haider et al., 1998b), the direct imaging, with a single image, of atomic columns can be achieved. This holds not only for strongly scattering atoms but also for weakly scattering atoms, even when they are close to strongly scattering atoms. This is achieved employing the novel imaging mode obtained by adjusting the spherical aberration of the objective lens for a small negative value. Combining this with an appropriate value of overfocus, high-quality bright-atom contrast is obtained. This contrast enhancement can be explained in the framework of a fully dynamic nonlinear quantum mechanical contrast theory.

## References

Coene, W. & Jansen, A.J.E.M. (1992). Image delocalisation and high resolution transmission electron microscopic imaging with a field emission gun. *Scanning Microsc* (Suppl. 6), 379–403.

Coene, W., Janssen, G., Op de Beeck, M. & Van Dyck, D. (1992). Phase retrieval through focus variation for ultra-resolution in field-emission transmission electron microscopy. *Phys Rev Lett* **69**, 3743–3746.

Haider, M., Rose, H., Uhlemann, S., Kabius, B. & Urban, K. (1998a). Towards 0.1 nm resolution with the first spherically corrected transmission electron microscope. *J Electron Microsc* **47**, 395–405.

Haider, M., Rose, H., Uhlemann, S., Schwan, E., Kabius, B. & Urban, K. (1998b). Electron microscopy image enhanced. *Nature* **392**, 768–769.

Haider, M., Rose, H., Uhlemann, S., Schwan, E., Kabius, B. & Urban, K. (1998c). A spherical-aberration-corrected 200 kV transmission electron microscope. *Ultramicroscopy* **75**, 53–60.

Heinemann, K. (1971). In-situ measurement of objective lens data of a high-resolution electron microscope. *Optik* **34**, 113–128.

Horiuchi, S., Matsui, Y., Kitami, Y., Yokoyama, M., Suehara, S., Wu, X.J., Matsui, I. & Katsuta, T. (1991). Ultra-high-resolution HVEM (H-1500) newly constructed at NIRIM. II. Application to materials. *Ultramicroscopy* **39**, 231–237.

Huxford, N.P., Eaglesham, D.J. & Humphreys, C.J. (1987). Limits on quantitative information from high-resolution electron microscopy of YBa$_2$Cu$_3$O$_7$ superconductors. *Nature* **329**, 812–813.

Jia, C.L., Lentzen, M. & Urban, K. (2003). Atomic-resolution imaging of oxygen in perovskite ceramics. *Science* **299**, 870–873.

Jia, C.L. & Thust, A. (1999). Investigation of atomic displacements at a $\Sigma 3$ {111} twin boundary in BaTiO$_3$ by means of phase-retrieval electron microscopy. *Phys Rev Lett* **82**, 5052–5055.

Jorgensen, D., Beno, M.A., Hinks, D.G., Soderholm, L., Volin, K.J., Hitterman, R.L., Grace, J.D., Schuller, I.K., Segre, C.U., Zhang, K. & Kleefisch, M.S. (1987). Oxygen ordering and the orthorhombic-to-tetragonal phase transition in YBa$_2$Cu$_3$O$_{7-x}$. *Phys Rev B* **36**, 3608–3616.

Kilaas, R. (1987). Interactive simulation of high resolution electron micrographs. In *Proceedings of the 45th Annual EMSA Meeting*, Bailey, G.W. (Ed.), pp. 66–67. San Francisco, CA: San Francisco Press.

Kisielowski, C., Hetherington, C.J.D., Wang, Y.C., Kilaas, R., O'Keefe, M.A. & Thust, A. (2001). Imaging columns of the light elements carbon, nitrogen and oxygen with sub Ångstrom resolution. *Ultramicroscopy* **89**, 243–263.

Krekels, T., Van Tendeloo, G. & Amelinckx, S. (1991). Oxygen-

vacancy ordering in $Y_2Ba_4Cu_7O_{15-\epsilon}$. *Appl Phys Lett* **59**, 3048–3050.

Lentzen, M., Jahnen, B., Jia, C.L., Thust, A., Tillmann, K. & Urban, K. (2002). High-resolution imaging with an aberration-corrected transmission electron microscope. *Ultramicroscopy* **92**, 233–242.

Lichte, H. (1991). Optimum focus for taking electron holograms. *Ultramicroscopy* **38**, 13–22.

Morris, D.E., Asmar, N.G., Wei, J.Y.T., Nickel, J.H., Sid, R.L., Scott, J.S. & Post, J.E. (1989). Synthesis and properties of the 2:4:7 superconductors $R_2Ba_4Cu_7O_{15-x}$ ($R$ = Y, Eu, Gd, Dy, Ho, Er). *Phys Rev B* **40**, 11406–11409.

Ohtomo, A., Muller, D.A., Grazul, J.L. & Hwang, H.Y. (2002). Artificial charge-modulation in atomic-scale perovskite titanate superlattices. *Nature* **419**, 378–380.

O'Keefe, M.A., Hetherington, C.J.D., Wang, Y.C., Nelson, E.C., Turner, J.H., Kisielowski, C., Malm, J.-O., Mueller, R., Ringnalda, J., Pan, M. & Thust, A. (2001). Sub-Ångstrom high-resolution transmission electron microscopy at 300 keV. *Ultramicroscopy* **89**, 215–241.

Ourmazd, A. & Spence, J.C.H. (1987). Detection of oxygen ordering in superconducting cuprates. *Nature* **329**, 425–427.

Pennycook, S.J., Jesson, D.E., Nellist, P.D., Chrisholm, M.F. & Browning, N.D. (1997). Scanning Transmission Electron Microscopy: Z-Contrast. In *Handbook of Microscopy*, Vol. II, Amelinckx, S., Van Dyck, D., Van Landuyt, J.F. & Van Tendeloo, G. (Eds.), pp. 595–620. Weinheim, Germany: Wiley-VCH.

Poole, C.P., Farach, H.A. & Creswick, R.J. (1995). *Superconductivity*. San Diego, CA: Academic Press.

Rose, H. (1990). Outline of a spherically corrected semiaplanatic medium-voltage transmission electron microscope. *Optik* **85**, 19–24.

Scherzer, O. (1949). The theoretical resolution limit of the electron microscope. *J Appl Phys* **20**, 20–29.

Stadelmann, P.A. (1987). EMS—A software package for electron diffraction analysis and HREM image simulation in materials science. *Ultramicroscopy* **21**, 131–145.

Tagantsev, A.K., Stolichnov, I., Colla, E.L. & Setter, N. (2001). Polarization fatigue in ferroelectric films: Basic experimental findings, phenomenological scenarios, and microscopic features. *J Appl Phys* **90**, 1387–1402.

Urban, K., Kabius, B., Haider, M. & Rose, H. (1999). A way to higher resolution: Spherical-aberration correction in a 200 kV transmission electron microscope. *J Electron Microsc* **48**, 821–826.

Van Tendeloo, G. & Krekels, T. (2000). Identification of new superconducting compounds by electron microscopy. In *Characterization of High $T_C$ Materials & Devices by Electron Microscopy*, Browning, N.D. & Pennycook, S.J. (Eds.), pp. 161–191. Cambridge, UK: Cambridge University Press.

Waser, R. (1997). Dielectric analysis of integrated ceramic thin film capacitors. *Integr Ferroelect* **15**, 39–51.

Yan, Y. & Blanchin, M.G. (1991). Direct imaging of the oxygen sublattice in $YBa_2Cu_3O_{7-\delta}$ superconductors by high-resolution electron microscopy. *Phys Rev B* **43**, 13717–13719.

Zandbergen, H.W., Gronsky, R., Wang, K. & Thomas, G. (1988). Structure of $(CuO)_2$ double layers in superconducting $YBa_2Cu_3O_7$. *Nature* **331**, 596–599.